

Evidence for Ultra-Low Velocity Zone Genesis in Downwelling Subducted Slabs at the Core–Mantle Boundary

Madeleine M. Festin¹, Michael S. Thorne^{*1}, and Mingming Li²

Abstract

We investigate broadband *SPdKS* waveforms from earthquakes occurring beneath Myanmar. These paths sample the core–mantle boundary beneath northwestern China. Waveform modeling shows that two $\sim 250 \times 250$ km wide ultra-low velocity zones (ULVZs) with a thickness of roughly 10 km exist in the region. The ULVZ models fitting these data have large *S*-wave velocity drops of 55% but relatively small 14% *P*-wave velocity reductions. This is almost a 4:1 *S*- to *P*-wave velocity ratio and is suggestive of a partial melt origin. These ULVZs exist in a region of the Circum-Pacific with a long history of subduction and far from large low-velocity province (LLVP) boundaries where ULVZs are more commonly observed. It is possible that these ULVZs are generated by partial melting of mid-ocean ridge basalt.

Cite this article as Festin, M. M., M. S. Thorne, and M. Li (2024). Evidence for Ultra-Low Velocity Zone Genesis in Downwelling Subducted Slabs at the Core–Mantle Boundary, *The Seismic Record*, **4**(2), 111–120, doi: [10.1785/0320240003](https://doi.org/10.1785/0320240003).

Supplemental Material

Introduction

Ultra-low velocity zones (ULVZs) are thin patches of material with reduced seismic wavespeeds sitting on top of the core–mantle boundary (CMB). Most efforts at ULVZ characterization infer either a partially molten (e.g., Williams and Garnero, 1996; Revenaugh and Meyer, 1997) or Fe-enriched compositional origin to the ULVZs (e.g., Muir and Brodholt, 2015; Wicks *et al.*, 2017; Krier *et al.*, 2021). Previous efforts have suggested that ULVZs may be preferentially found beneath hot spot volcanoes (e.g., Jenkins *et al.*, 2021; Cottaar *et al.*, 2022) or along large low-velocity province (LLVP) boundaries (e.g., Li *et al.*, 2017; Fan *et al.*, 2022; Lai *et al.*, 2022). But ULVZs are also found in the Circum-Pacific region (Havens and Revenaugh, 2001; Thorne *et al.*, 2019, 2020, 2021)—a region inferred to be associated with the resting place of subducted slabs (e.g., Grand, 2002). Recent studies suggest that different mineral phases have the potential to transport water to the CMB (see Walter, 2021 for a review). In this case, water released could introduce melting in the mantle or even react with outer core Fe to produce a dense low-velocity phase (Mao *et al.*, 2017). Mid-ocean ridge basalt (MORB) in subducted slab crust could potentially melt when heated up at the CMB, serving as another possible source of melt

(e.g., Andrault *et al.*, 2014). Thus, a natural place to search for ULVZ genesis could be at the margins of subducted materials.

We use the *SPdKS* seismic phase to further investigate a ULVZ located beneath northwestern China identified previously (Thorne *et al.*, 2020, 2021). The *SPdKS* phase is an *S* wave that intersects the CMB at the critical angle for *P*-wave diffraction (Fig. 1). These legs of *P* diffraction are sensitive to structures along the CMB. Here, we analyze *SPdKS* data crossing this region using a waveform modeling approach and demonstrate that the seismic waveforms for these data are consistent with a partially molten ULVZ origin. In addition, geodynamic modeling constrained by the past 200 million years of subduction (Seton *et al.*, 2012) suggests that MORB material is likely being

1. Department of Geology and Geophysics, University of Utah, Salt Lake City, Utah, U.S.A., <https://orcid.org/0009-0006-6511-9987> (MMF); <https://orcid.org/0000-0002-7087-1771> (MST); 2. School of Earth and Space Exploration, Arizona State University, Tempe, Arizona, U.S.A., <https://orcid.org/0000-0003-4335-5066> (ML)

*Corresponding author: michael.thorne@utah.edu

© 2024. The Authors. This is an open access article distributed under the terms of the CC-BY license, which permits unrestricted use, distribution, and reproduction in any medium, provided the original work is properly cited.

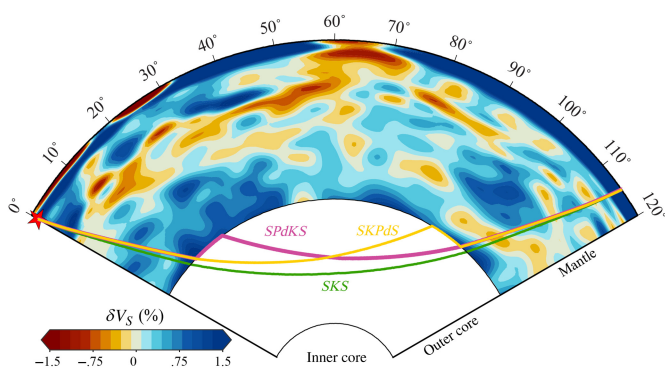


Figure 1. Ray paths for *SPdKS* (magenta), *SKPdS* (yellow), and *SKS* (green) for a 136 km deep source (red star) to a receiver at 115° in epicentral distance. The background is the *S*-wave tomography model S40RTS (Ritsema *et al.*, 2011). The cross-section begins at 23.09° N, 94.8654° E and ends at 37° N, 89° W for an epicentral distance of about 120°.

transported to the CMB in this region. If this MORB material is undergoing melting, ULVZs could be generated here.

Data and Methods

Seismic data were collected as a part of two previous studies (Thorne *et al.*, 2020, 2021). This collection consisted of over 270,000 high-quality seismograms for events occurring between 1990 and 2017 with event depths ≥ 75 km in the epicentral distance range from 90° to 130°. Details on data collection and processing steps are given in Thorne *et al.* (2020) but include standard processing steps such as (1) removing instrument response, (2) rotating to the radial component, and (3) integrating to displacement.

We selected events that crossed a probable ULVZ target zone in East Asia (Thorne *et al.*, 2020, 2021) and identified seven events from 1995 to 2017 with $M_w \geq 5.8$ and depths > 75 km with simple source time functions (see Table S1, available in the supplemental material to this article). We searched for additional recent events, but no high-quality events occurred in this region since 2017. For these events, we obtained 2307 total records. The location of events and receivers used are shown in Figure 2. Three of these events had many records spanning both a wide azimuthal and epicentral distance range, which we focus on here: (1) 3 September 2009 (19:51), (2) 13 April 2016 (13:55), and (3) 24 August 2016 (10:34). Distance profiles for these events are provided in the supplemental material (Figs. S1–S10).

We reviewed each trace in the epicentral distance range from 108° to 115° and categorized them as either anomalous or not anomalous (Thorne *et al.*, 2019, 2020). In typical preliminary reference Earth model-like (PREM) records in this distance

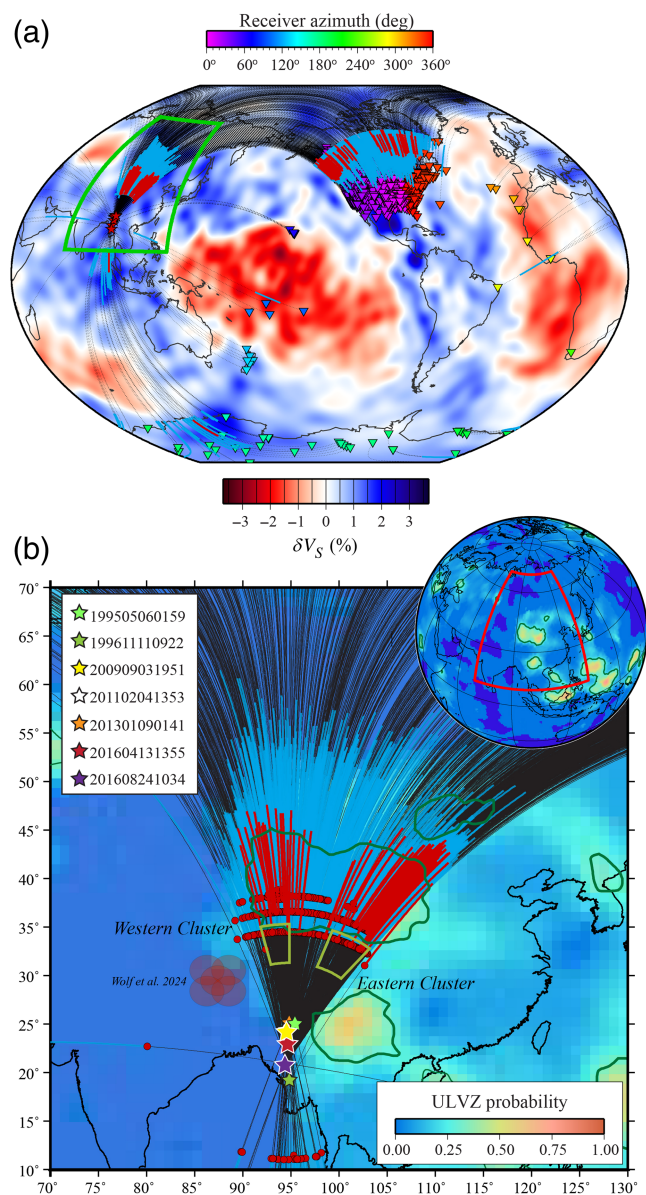


Figure 2. (a) The global distribution of anomalous (red) and nonanomalous (blue) core–mantle boundary (CMB) *Pd* paths for both source and receiver side diffraction. Black dotted curves represent the great circle path between sources (red stars) and receivers (triangles). The background is *S*-wave tomography from model S40RTS at a depth of 2890 km (Ritsema *et al.*, 2011). The green box shows the source-side area detailed in panel (b). (b) Great-circle paths from the source (stars) to the receiver are thin black curves with the normal CMB *Pd* segments in blue. Anomalous *Pd* paths are in red. The points at which *Pd* starts to diffract along the CMB (the *Pd* inception points) are drawn as red circles. The background is ultra-low velocity zone (ULVZ) likelihood (Thorne *et al.*, 2021). Contours are drawn at a probability of 0.25 (green) and highlight the areas with the highest probability of ULVZ existence. Yellow boxes show ULVZ locations inferred from 2.5D waveform modeling. Light-shaded red circles show the inferred ULVZ position from (2024). The inset shows the study region outlined in red in a global view. The background is the ULVZ likelihood (Thorne *et al.*, 2021).

range, either *SKS* exists alone, or at epicentral distances roughly greater than 111° , *SPdKS* also starts to emerge from the shoulder of *SKS* with a lower amplitude than *SKS*. Thus, in nonanomalous waveforms, we observe either 1 or 2 arrivals; and when we observe 2 arrivals, the second arrival has a lower amplitude than the first. Here, records were identified as anomalous if they had an additional arrival (e.g., 2 or 3 arrivals when only 1 or 2 are expected) or if the second arrival emerged with a larger amplitude than the first. The locations of the anomalous and nonanomalous ray paths on the CMB are shown in Figure 2a,b. The anomalous records are concentrated in two azimuthal bands with relatively normal waveforms located between them. All anomalous waveforms overlie areas of high seismic velocity in tomographic models on both source and receiver sides of the path (Fig. 2a). The concentrations of anomalous waveforms on the source side of the path are consistent with ULVZ-like-likelihood calculations of Thorne *et al.* (2021; see Fig. 2b). For the concentration of anomalous waveforms to the east, a second high-likelihood zone exists near the *Pd* path exit, perhaps indicating complex ULVZ structure on the source side of the path.

On the receiver side of the path, *Pd* segments are widely distributed (Fig. 2a). Following the interpretation of 3D synthetic seismograms by Thorne *et al.* (2021), it is likely that anomalous structure giving rise to these anomalous waveforms is concentrated near the source. Otherwise, anomalous structures would be spread out over several thousand kilometers beneath North America (see figs. 3–5 in Thorne *et al.*, 2021).

We sorted records into 6° wide azimuthal bins, which divided areas of anomalous and nonanomalous waveforms yet also provided enough waveforms in each bin to obtain quality waveform stacks. Records were sorted into 1° epicentral distance bins, band-pass filtered with corners between 0.025 and 1.0 Hz, and stacked using the adaptive stacking algorithm of Rawlinson and Kennett (2004).

Example waveforms for an event occurring on 13 April 2016 are shown in Figure 3. This figure shows waveforms for three different azimuthal bands that are representative of the waveform behavior encountered in this region. In Figure 3a, seismic traces for the western cluster of anomalous waveforms are represented in the azimuth band from 354° to 360° . The waveform stacks (blue) from epicentral distances 111° – 115° show clear waveform differences from the PREM synthetics (green). In Figure 3b, data for the central region are shown (azimuths 0° – 6°). These waveforms are similar to the PREM predictions. The eastern region, azimuths 24° – 30° , shows a high degree of complexity starting at an epicentral distance of 111° . Three

distinct arrivals are evident between 112° and 116° , and the waveforms are consistently distinct from PREM. In all the three azimuthal bins waveforms are matched well by PREM predictions for distances less than $\sim 110^\circ$, indicating a simple source time function. For distances greater than 120° , the waveforms are also similar to PREM. At large epicentral distances, *SPdKS* waveforms commonly look similar to PREM, which has been previously noticed in global studies (Thorne and Garnero, 2004). This similarity may be related to wavefront healing of the long *Pd* path around ULVZs but is not evident in all locations (e.g., beneath the Coral Sea Jensen *et al.*, 2013), which may provide important evidence toward ULVZ size. Waveform stacks compared to PREM are shown for all azimuthal bins in the supplemental material (Figs. S11–S18) as well as individual waveforms in the most highly anomalous regions (Figs. S19, S20).

Data stacks were compared to synthetic seismograms computed with the PSVaxi technique (e.g., Vanacore *et al.*, 2016; Krier *et al.*, 2021). The primary model space is computed for boxcar-shaped models (Fig. 3d) on a regular grid.

- ULVZ thicknesses (h) ranging from 5 to 45 km in 5 km increments.
- ULVZ length (l) in the great circle arc direction of 0.75° , 1.5° , 3.0° , 6.0° , 9.0° , and 12.0° .
- ULVZ edge position (l_1) from 5.5° to 29.5° in 1.5° increments.
- *S*-wave velocity reductions (δV_S) of -10% , -20% , -30% , -40% , and -50% with respect to the PREM.
- *P*-wave velocity reductions (δV_P) of -10% , -20% , -30% , -40% , and -50% with respect to the PREM, noting that we never allow δV_P reductions to be larger than δV_S .

Additional models exist in our model space for source-side ULVZ geometries that have been computed for various studies (Jensen *et al.*, 2013; Thorne *et al.*, 2013, 2019; Krier *et al.*, 2021), giving a total of over 21,000 ULVZ models. *SPdKS* has minimal sensitivity to density (ρ), and in this model space, we fix it to $\rho = +10\%$ with respect to PREM (e.g., Rost *et al.*, 2005). All models are computed at a 500 km source depth and are shifted to a common source depth (see Thorne *et al.*, 2019).

We first compare data stacks in each azimuthal bin to synthetic seismograms from our precomputed model space. We create an empirical source wavelet for each event by stacking *SKS* waveforms in the epicentral distance range from 90° to 105° . Then, we do a grid search through triangle and truncated triangle functions such that when it is convolved with the PSVaxi synthetics we match the *SKS* waveforms for that event

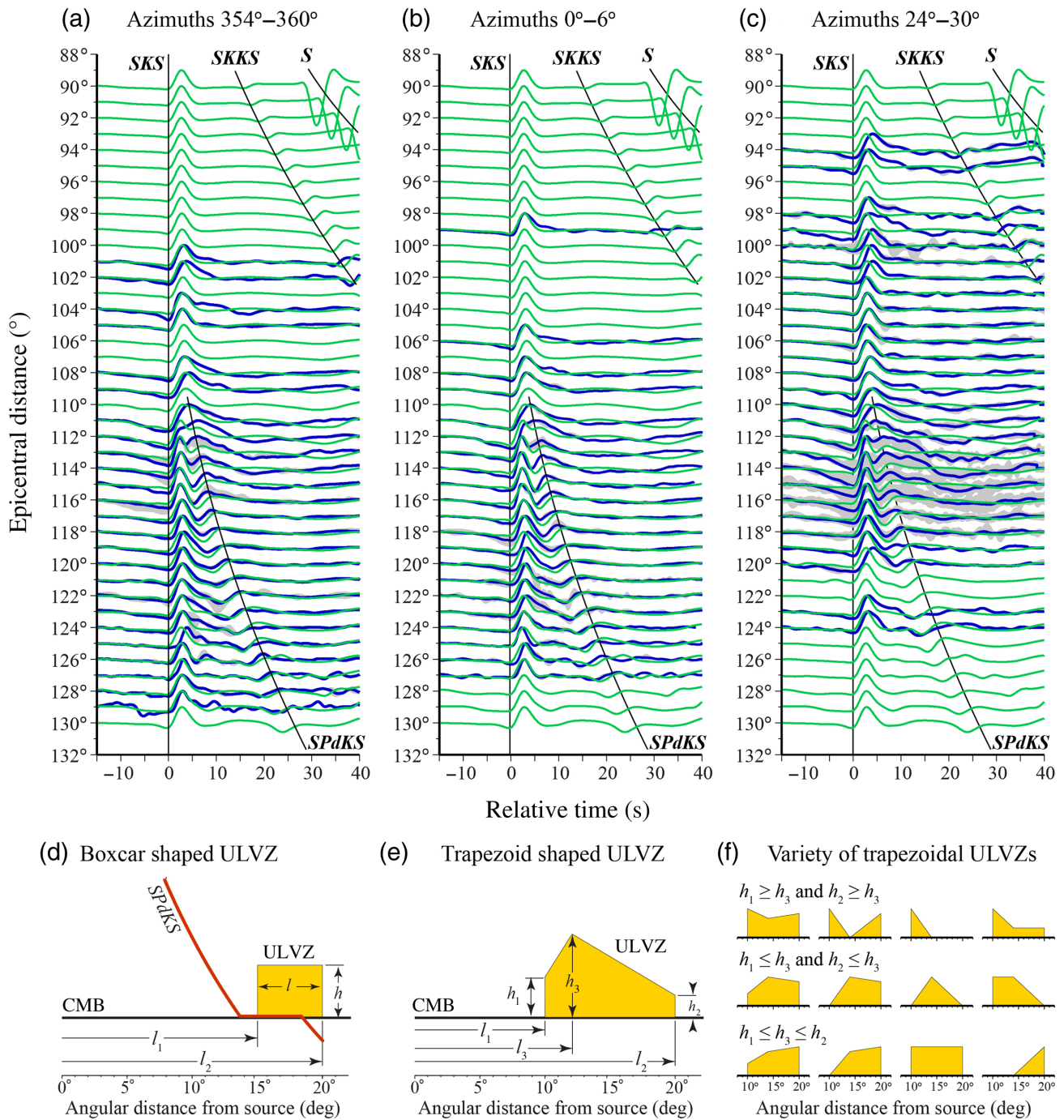


Figure 3. Seismic waveforms from the event occurred on 13 April 2016, at a depth of 136 km. Individual panels show traces for a narrow azimuth range from (a) 354°–360°, (b) 0°–6°, and (c) 24°–30°. In each panel, the data stack is shown in blue, which overlays the preliminary reference Earth model (PREM) synthetic seismograms in green. The gray shaded region shows the variation amplitude of all arrivals that went into the stack at that distance. All seismograms are radial component displacement traces aligned and normalized to unity on the *SKS* arrival. Waveforms are band-pass filtered with corners between 0.025 and 1.0 Hz. (d) Model geometry

for boxcar-shaped ULVZs. ULVZ location (yellow box) with $l = 5^\circ$, starting at an edge position of $l_1 = 15^\circ$ and ending at $l_2 = 20^\circ$. ULVZ thickness is given by h . The red trace shows an *SPdKS* ray for an epicentral distance of 108° . (e) Model geometry for trapezoidal-shaped ULVZ with $l_1 = 10^\circ$, $l_2 = 20^\circ$, and $l_3 = 12^\circ$. (f) A variety of ULVZ shapes can be realized with the trapezoidal model. Here, the values of $l_1 = 10^\circ$, $l_2 = 20^\circ$, and $l_3 = 14^\circ$ are fixed to show that in addition to a variety of trapezoids, this model parameterization also generates boxcar and triangle-shaped models. Not all possibilities are shown here. CMB, core–mantle boundary.

(see Thorne and Garnero, 2004 for a detailed description of generating the empirical source). All data stacks are aligned such that the SKS arrival starts at zero seconds. Then, we find the best shift for the synthetic seismogram to match the data stack using cross-correlation. For each synthetic-data pair, we compute the cross-correlation coefficient (CC) for the best-shifted seismogram over the interval from -5 to $+30$ s. The time window was chosen to include possible ULVZ-related precursors to SKS (i.e., SPKS) and additional postcursors that exist in many of the ULVZ models. We also integrate the synthetic and data trace over the same interval and compute an integral goodness of fit (IGF) measurement defined as

$$\text{IGF} = 1.0 - \frac{|\int_{-5}^{30} \text{data}(t)dt - \int_{-5}^{30} \text{synthetic}(t)dt|}{\int_{-5}^{30} \text{synthetic}(t)dt}. \quad (1)$$

We define our goodness of fit (GF) as the CC multiplied by the integral (IGF). This is averaged over all distances for which we have data stacks, to get a single number for each synthetic model:

$$\text{GF}(\text{synthetic model}) = \frac{1}{n} \sum_{i=1}^n \text{IGF}(i) \times \text{cc}(i), \quad (2)$$

in which we have n data stacks in the azimuth window.

We use the results from the comparisons with the boxcar models as a starting point to compare data with more complicated trapezoidal ULVZ models (Fig. 3e). We introduce an additional length parameter (l_3) that can lie anywhere in between the l_1 and l_2 edges. We allow the height to be adjustable at each angular location and have three height parameters: h_1 (at the l_1 edge), h_3 (at l_3 in between l_1 and l_2), and h_2 (at the l_2 edge). We allow any of the height parameters to be zero, allowing for a wide variety of ULVZ shapes (a sample is shown in Fig. 3f).

Results

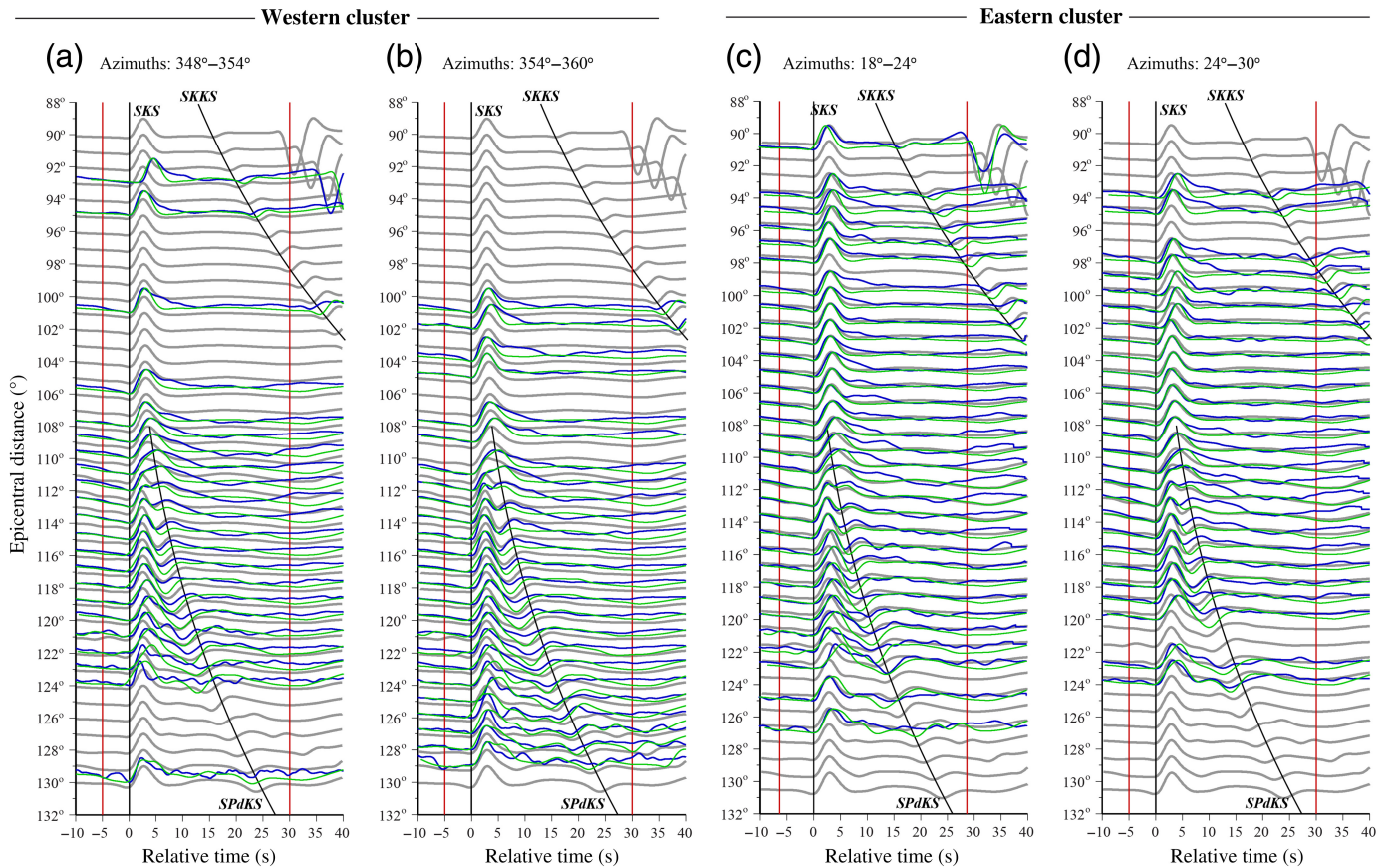
We computed a GF for each synthetic ULVZ model compared with each event, for each 6° azimuthal band. The highest quality event is the 13 April 2016 event, so we focus the discussion on this event, with waveform comparisons for the other two primary events shown in the supplemental material (Figs. S33–S36). We found that the models with the highest GF are consistent for the three regions, which for this event we define as: (1) the western cluster (azimuths from 348° to 360° and 0° to 6°), (2) the central cluster (azimuths from 6° to 18°), and (3) the eastern cluster (azimuths from 18° to 36°).

For both the eastern and western clusters, the best-fit model has ULVZ model parameters of $\delta V_S = -50\%$, $\delta V_P = -50\%$, $h = 45$ km, $l = 6^\circ$, and $l_1 = 5.5^\circ$. This model has elastic parameters at the extremes, but with an edge position of $l_1 = 5.5^\circ$, the point where Pd initiates on the CMB is near the far edge (the l_2 edge) of the ULVZ, and there is little interaction of the SPdKS wavefield with the ULVZ. This model predicts interesting wavefield complexity similar to observed data; but the extreme properties of this model predict unrealistically large-amplitude postcursors that we do not observe in any of our data if the ULVZ is moved such that the SPdKS wavefield has more interaction with the ULVZ (see Figs. S21, S22).

We also investigated histograms of ULVZ properties for the top-fitting models. The histograms reveal that both eastern and western clusters are consistently explained by models with mean values of $\delta V_S = -50\%$, δV_P from -20% to 0% , $h = 10$ km, $l = 1.5^\circ$ – 3° , and l_1 from 8.5° to 10° . The central cluster is dominated by small-length models with $\delta V_S = -10\%$ and $\delta V_P = 0\%$, which are the smallest P - and S -wave velocities in the model space and are identical to PREM predictions for lengths of $l = 0.75^\circ$ and edge positions $l_1 = 5.5^\circ$. This indicates ULVZ-like structure in the eastern and western clusters and a PREM-like structure in the central cluster (see histograms in Figs. S40–S46).

We refined the model further by conducting a grid search in the vicinity of the starting model with smaller step sizes between parameters. Our refined models showed ULVZ parameters in the eastern cluster with $\delta V_S = -55\%$, $\delta V_P = -14\%$, $h = 8$ km, $l = 2.5^\circ$, and $l_1 = 8.5^\circ$. For the western cluster we obtained: $\delta V_S = -56\%$, $\delta V_P = -14\%$, $h = 8$ km, $l = 1.75^\circ$, and $l_1 = 9.0^\circ$. Figures S23 and S24 show waveform comparisons for these ULVZ models compared to data. These models provide a good fit in the early portions of the waveform that includes SKS and SPdKS but do not fit the complexity of the SPdKS postcursor wavefield.

The added complexity of the postcursor wavefield could be fit by an arrival that emerges from the l_2 ULVZ edge. To explore this possibility, we generated a series of sensitivity tests (Figs. S25–S30). An additional postcursor is generated at the correct travel time to match our observations if the l_2 edge is located around 20° , but an additional negative polarity arrival gets generated from the l_1 edge, which destructively interferes with the SPdKS wavefield. Thorne et al. (2021) shows that SPdKS waveforms in the eastern cluster could be interacting with two distinct ULVZs. We tested models with two boxcar ULVZs located on the source side. These types of models fit



the character of the waveforms well (see Fig. S31). But similar to our previous experiments, a negative polarity arrival is generated at the l_1 edge that degrades the overall GF.

To test if we can fit the complexity of the waveforms without introducing a negative polarity arrival in the middle of the *SKS* and *SPdKS* wavefield, we tested a series of trapezoidal models (see Fig. 3e,f). We computed an additional 1500 models with fixed values of $\delta V_S = -55\%$ and $\delta V_P = -14\%$ based on our boxcar model results. We allowed all three thickness parameters (h_1 , h_3 , and h_2) to be 0, 5, 10, or 15 km. We allowed l_1 to be 8° or 9° ; l_2 to be 10° , 12° , 14° , or 16° ; and l_3 to be 12° , 14° , 16° , 18° , 20° , or 22° .

For the western cluster, we find that the model with the highest GF has length parameters of $l_1 = 8^\circ$, $l_3 = 10^\circ$, and $l_2 = 12^\circ$. Corresponding height parameters are $h_1 = 15$ km, $h_3 = 10$ km, and $h_2 = 5$ km. The waveform fits are shown in Figure 4a,b. For the eastern cluster, the model with the highest GF has length parameters of $l_1 = 8^\circ$, $l_3 = 10^\circ$, and $l_2 = 12^\circ$. Corresponding height parameters are $h_1 = 15$ km, $h_3 = 10$ km, and $h_2 = 5$ km. The waveform fit between this synthetic prediction and waveforms from the eastern cluster is shown in Figure 4c,d.

Figure 4. Seismic waveforms from the event occurring on 13 April 2016. Individual panels show traces for representative azimuth ranges for the western cluster (a) 354° – 360° , (b) 0° – 6° , and the eastern cluster (c) 18° – 24° and (d) 24° – 30° . In each panel, the data stack is shown in blue which overlie the ULVZ synthetic predictions in green. PREM synthetic predictions are shown in gray. All ULVZ synthetic predictions have $\delta V_S = -55\%$ and $\delta V_P = -14\%$. In panels (a) and (b) trapezoidal models are shown with $l_1 = 8^\circ$, $l_3 = 10^\circ$, and $l_2 = 12^\circ$ and height parameters of $h_1 = 15$ km, $h_3 = 10$ km, and $h_2 = 5$ km. In panels (c) and (d) models are shown with $l_1 = 8^\circ$, $l_3 = 10^\circ$, and $l_2 = 12^\circ$ and height parameters of $h_1 = 15$ km, $h_3 = 10$ km, and $h_2 = 5$ km. The vertical red lines show the time window in which data are compared with synthetics. All seismograms are radial component displacement traces aligned and normalized to unity on the *SKS* arrival. Waveforms are band-pass filtered with corners between 0.025 and 1.0 Hz.

These models fit the anomalous *SKS* and *SPdKS* portions of the wavefield at distances around 112° but underestimate the amplitude of the third arrival for the eastern cluster. A model with $l_1 = 8^\circ$, $l_3 = 10^\circ$, $l_2 = 14^\circ$ and $h_1 = 0$ km, $h_3 = 10$ km, and $h_2 = 10$ km visually appears to fit the eastern cluster data better with respect to the third arrival (Fig. S32) but still gives amplitudes that are too low in the central portion of the wavefield. The

locations of the inferred ULVZs based on the highest GF trapezoidal models are plotted in Figure 2b.

Discussion

We analyzed *SPdKS* seismic waveforms interacting with the ULVZ structure beneath northwestern China. These data reveal two thin (~10 km) ULVZ patches on the order of 250×250 km, separated by relatively PREM-like waveforms in between. We best model these waveforms with a trapezoidal ULVZ model (in 2.5D) to capture some of the waveform complexity characteristic of these data, but some of the waveforms contain greater complexity than displayed in the models we computed (see highly anomalous waveforms in Figs. S19, S20). It is possible that some of this complexity is caused by boundary interactions with 3D ULVZ structure because these ULVZs have finite extent in the lateral direction. The 3D nature of these ULVZs is supported by analyzing the absolute SKS arrival times for the study region (Figs. S37, S38). Here, we observe SKS arrival times that are delayed in the eastern and western azimuths concerning the PREM model but are fast in the central azimuthal band. The largest SKS delays occur for the eastern cluster and are as large as 5 s. Some of the SKS delay for this cluster can be attributable to low-seismic velocities on the receiver side of the path as is demonstrated in models of seismic tomography (Fig. S39); however, these models only predict roughly 2 s of delay, so a ULVZ as we predict in this location could account for the additional delay. The largest delays are observed for azimuths commensurate with the eastern and western clusters at the smallest latitudes, which also supports the ULVZ model occurring further to the south as inferred in this study (see Fig. 2). The 3D modeling efforts of small-scale ULVZs suggest that three arrivals could arise out of 3D ULVZ structure with an azimuthally dependent moveout (Thorne *et al.*, 2021). However, it is not clear from these data that such moveout exists in the third arrival. As fully 3D waveform modeling becomes more approachable future efforts should model this in full 3D (see e.g., Krier *et al.*, 2021).

The *S*- and *P*-wave velocity reductions we recovered for these ULVZs are -55% and -14% , respectively. This gives an *S*- to *P*-wave velocity ratio of nearly 4:1, which is suggestive of a partially molten origin to these ULVZs (Williams and Garnero, 1996). A recent study has demonstrated that iron-rich magnesiowüstite could also produce a 3:1 velocity ratio as an alternative to the partial melt hypothesis in certain cases (Dobrosavljevic *et al.*, 2019). However, this is only indicated for relatively small *S*-wave velocity decreases. For *S*-wave velocity decreases with

magnitudes larger than 30%, as we infer in this study, a 1:1 to 2:1 velocity ratio is predicted for the iron-rich compositional case. Modeling in 3D geometries may give different elastic parameters than those we recovered here because, in the 2.5D simulations, the energy is focused differently than in 3D (Krier *et al.*, 2021). But in considering over 20,000 2.5D ULVZ models the best-fitting models predominantly had 3:1 or 4:1 *S*- to *P*-wave velocity ratios, and thus these ULVZs are excellent candidates for a partially molten origin.

Another recent study found a ULVZ adjacent to our westernmost ULVZ using the S_{diff} seismic phase (location is indicated in Fig. 2) and also inferred a large *S*-wave velocity decrease of between 32% and 40% with a fixed 20 km thickness (Wolf *et al.*, 2024). Trade-offs exist between ULVZ thickness, *S*-wave velocity reduction, and size, and hence the ULVZ imaged by Wolf *et al.* (2024) may have a similarly large velocity reduction if they cut their ULVZ thickness by half commensurate with our modeling. It is unclear if the ULVZ we observe in the western cluster is a distinct ULVZ or an extension of the ULVZ imaged by Wolf *et al.* (2024) as we lack sufficient overlapping *SPdKS* coverage.

Typically, partially molten ULVZs are expected to exist in the hottest part of the lower mantle, such as the interiors of the LLVPs (Li *et al.*, 2017). However, the ULVZs in this study occur in a region far from the LLVPs and beneath long-term subduction. Hansen *et al.* (2023) used tracers to track the subducted materials in global mantle convection models and showed that regions beneath subduction outside the LLVPs in the lowermost mantle could contain widespread subducted materials. Here, we further analyzed the convection model of Hansen *et al.* (2023). We introduce passive tracers at 300 km depth beneath subduction regions during four different time periods of 200–150, 150–100, 100–50, and 50–0 Ma. Once introduced to the model domain, the tracers are advected with mantle flow to the deeper interiors (Movie S1). We find that subducted materials sink vertically at most depths; but they spread out laterally in the lowermost mantle. The majority of subducted materials that reach the base of mantle in our study region at the present day are those that are introduced to the model domain between 150 and 100 Ma at the western Pacific subduction zones (Fig. 5a–c, panel b in Movie S1). The model shows that our study region is generally colder than regions beneath the central Pacific and Africa where the LLVPs are located (Fig. 5d) and contains widespread subducted materials in the lowermost 100 km of the mantle (Fig. 5e,f, Movie S2).

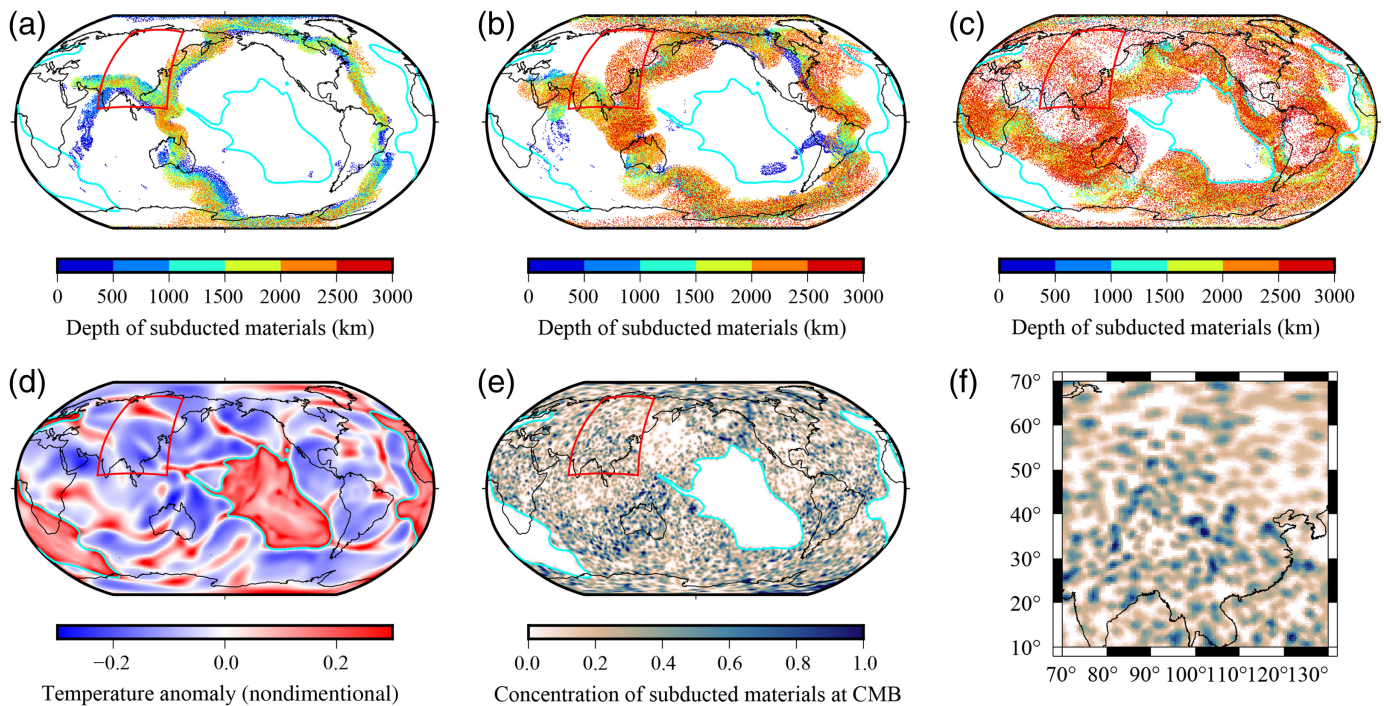


Figure 5. (a–c) Distribution of subducted materials in the deep mantle at (a) 120 Ma, (b) 88 Ma, and (c) present-day. The subducted materials are represented by passive tracers that are advected with mantle flow. These tracers are consistently introduced to the model domain at 300 km depth beneath the subduction region during the time periods of 150–100 Ma. A complete video for panels (a–c) is shown in Movie S1. The color shows the depth of the tracers. (d) Present-day temperature anomaly at 40 km above the CMB. (e) The present-day distribution of subducted materials in the lowermost 100 km of the mantle is calculated by the relative number of passive tracers per area in this depth range. The red boxes in panels (d) and (e) identify the seismic study region. The cyan contours show boundaries of thermochemical piles that represent the large low-velocity provinces (LLVPs) in the model. (f) Zoomed-in view of the panel (e) in our study region. A complete video for panels (d–f) is shown in Movie S2.

We note that the mantle convection model discussed earlier does not distinguish between subducted MORB and subducted lithospheric mantle. Mineral physics experiments have suggested that subducted MORB has higher intrinsic density than the surrounding mantle (e.g., Hirose *et al.*, 2005) and could segregate from subducted slabs when it reaches the lowermost mantle (e.g., Tackley, 2011; Li, 2023). The subducted MORB is at the top of subducted slabs and could even directly contact the CMB before crustal segregation occurs (Li, 2023). During its migration along the CMB, the MORB could be shaped into accumulations with variable shapes (Li, 2023).

Conclusions

We show additional evidence that ULVZs can be found beneath areas of subduction in the Circum-Pacific. The most anomalous *SPdKS* waveforms observed in this region show as much complexity as those observed for a ULVZ beneath northern Mexico, also in a region of long-standing subduction (Thorne *et al.*, 2019). In both locations, waveform modeling suggests 4:1 *S*- to *P*-wave velocity reductions, which could indicate a partially molten ULVZ. The ULVZs in our study region could be explained by partial melting of subducted MORB. The MORB has a relatively low melting temperature and may be partially molten at the CMB (e.g., Hirose *et al.*, 1999; Andrault *et al.*, 2014) and cause a significant reduction of seismic velocities (e.g., Williams and Garnero, 1996).

Data and Resources

All seismic recordings used in this study are available in the repository (doi: [10.7278/S50d-7n1m-4fdp](https://doi.org/10.7278/S50d-7n1m-4fdp)). The supplemental material include plots of data used in this study, synthetic ULVZ predictions, and comparisons between data and synthetics.

Declaration of Competing Interests

The authors acknowledge that there are no conflicts of interest recorded.

Acknowledgments

The authors acknowledge the University of Utah Center for High Performance Computing (CHPC) for computing resources and

support. M. T. and M. F. were partially supported by the National Science Foundation (NSF) Grant Numbers EAR-1723081 and EAR-2139966. M. F. was also supported through the University of Utah Undergraduate Research Opportunities Program (UROP). M. L. was supported by NSF Grant Number EAR-2216564. Tomography models were obtained from the SubMachine utilities (Hosseini *et al.*, 2018). The authors thank Deputy Editor-in-Chief Vera Schulte-Pelkum, Stuart Russell, and an anonymous reviewer for constructive comments that improved this article.

References

- Andraut, D., G. Pesce, M. A. Bouhifd, N. Bolfan-Casanova, J.-M. Hénot, and M. Mezouar (2014). Melting of subducted basalt at the core-mantle boundary, *Science* **344**, 892–895, doi: [10.1126/science.1250466](https://doi.org/10.1126/science.1250466).
- Cottaar, S., C. Martin, Z. Li, and R. Parai (2022). The root to the Galapagos mantle plume on the core-mantle boundary, *Seismica* **1**, doi: [10.26443/seismica.v1i1.197](https://doi.org/10.26443/seismica.v1i1.197).
- Dobrosavljevic, V. V., W. Sturhahn, and J. M. Jackson (2019). Evaluating the role of iron-rich (Mg,Fe)O in ultralow velocity zones, *Minerals* **9**, doi: [10.3390/min9120762](https://doi.org/10.3390/min9120762).
- Fan, A., X. Sun, Z. Zhang, P. Zhang, and J. Zong (2022). From subduction to LLSVP: The core-mantle boundary heterogeneities across North Atlantic, *Geochem. Geophys. Geosys.* **23**, doi: [10.1029/2021GC009879](https://doi.org/10.1029/2021GC009879).
- Grand, S. P. (2002). Mantle shear-wave tomography and the fate of subducted slabs, *Philos. Trans. Roy. Soc. Lond. A* **360**, 2475–2491, doi: [10.1098/rsta.2002.1077](https://doi.org/10.1098/rsta.2002.1077).
- Hansen, S. E., E. J. Garnero, M. Li, S.-H. Shim, and S. Rost (2023). Globally distributed subducted materials along the Earth's core-mantle boundary: Implications for ultralow velocity zones, *Sci. Adv.* **9**, doi: [10.1126/sciadv.add4838](https://doi.org/10.1126/sciadv.add4838).
- Havens, E., and J. Revenaugh (2001). A broadband seismic study of the lowermost mantle beneath Mexico: Constraints on ultralow velocity zone elasticity and density, *J. Geophys. Res.* **106**, 30,809–30,820, doi: [10.1029/2000JB000072](https://doi.org/10.1029/2000JB000072).
- Hirose, K., Y. Fei, Y. Ma, and H.-K. Mao (1999). The fate of subducted basaltic crust in the Earth's lower mantle, *Nature* **397**, 53–56, doi: [10.1038/16225](https://doi.org/10.1038/16225).
- Hirose, K., N. Takafuji, N. Sata, and Y. Ohishi (2005). Phase transition and density of subducted MORB crust in the lower mantle, *Earth Planet. Sci. Lett.* **237**, 239–251.
- Hosseini, K., K. J. Matthews, K. Sigloch, G. E. Shephard, M. Domeier, and M. Tsekhmistenko (2018). SubMachine: Web-based tools for exploring seismic tomography and other models of Earth's deep interior, *Geochem. Geophys. Geosys.* **19**, 1464–1483, doi: [10.1029/2018GC007431](https://doi.org/10.1029/2018GC007431).
- Jenkins, J., S. Mousavi, Z. Li, and S. Cottaar (2021). A high-resolution map of Hawaiian ULVZ morphology from ScS phases, *Earth Planet. Sci. Lett.* **563**, doi: [10.1016/j.epsl.2021.116885](https://doi.org/10.1016/j.epsl.2021.116885).
- Jensen, K. J., M. S. Thorne, and S. Rost (2013). SPdKS analysis of ultralow-velocity zones beneath the western Pacific, *Geophys. Res. Lett.* **40**, 4574–4578, doi: [10.1002/grl.50877](https://doi.org/10.1002/grl.50877).
- Krier, J., M. S. Thorne, K. Leng, and T. Nissen-Meyer (2021). A compositional component to the Samoa ultralow-velocity zone revealed through 2- and 3-D waveform modeling of SKS and SKKS differential travel-times and amplitudes, *J. Geophys. Res.* **126**, doi: [10.1029/2021JB021897](https://doi.org/10.1029/2021JB021897).
- Lai, V. H., D. V. Helmberger, V. V. Dobrosavljevic, W. Wu, D. Sun, J. M. Jackson, and M. Gurnis (2022). Strong ULVZ and slab interaction at the northeastern edge of the Pacific LLSVP favors plume generation, *Geochem. Geophys. Geosys.* **23**, doi: [10.1029/2021GC010020](https://doi.org/10.1029/2021GC010020).
- Li, M. (2023). Variable distribution of subducted oceanic crust beneath subduction regions of the lowermost mantle, *Phys. Earth Planet. In.* **341**, doi: [10.1016/j.pepi.2023.107063](https://doi.org/10.1016/j.pepi.2023.107063).
- Li, M., A. K. McNamara, E. J. Garnero, and S. Yu (2017). Compositionally-distinct ultra-low velocity zones on Earth's core-mantle boundary, *Nat. Commun.* **8**, 177, doi: [10.1038/s41467-017-00219-x](https://doi.org/10.1038/s41467-017-00219-x).
- Mao, H.-K., Q. Hu, L. Yang, J. Liu, D. Y. Kim, Y. Meng, L. Zhang, V. B. Prakapenka, W. Yang, and W. L. Mao (2017). When water meets iron at Earth's core-mantle boundary, *Natl. Sci. Rev.* **4**, 870–878, doi: [10.1093/nsr/nwx109](https://doi.org/10.1093/nsr/nwx109).
- Muir, J. M. R., and J. P. Brodholt (2015). Elastic properties of ferropericlase at lower mantle conditions and its relevance to ULVZs, *Earth Planet. Sci. Lett.* **417**, 40–48, doi: [10.1016/j.epsl.2015.02.023](https://doi.org/10.1016/j.epsl.2015.02.023).
- Rawlinson, N., and B. L. N. Kennett (2004). Rapid estimation of relative and absolute delay times across a network by adaptive stacking, *Geophys. J. Int.* **157**, 332–340, doi: [10.1111/j.1365-246X.2004.02188.x](https://doi.org/10.1111/j.1365-246X.2004.02188.x).
- Revenaugh, J., and R. Meyer (1997). Seismic evidence of partial melt within a possibly ubiquitous low-velocity layer at the base of the mantle, *Science* **277**, 670–673.
- Ritsema, J., A. Deuss, H.-J. van Heijst, and J. H. Woodhouse (2011). S40RTS: A degree-40 shear-velocity model for the mantle from new Rayleigh wave dispersion, teleseismic travel time and normal-mode splitting function measurements, *Geophys. J. Int.* **184**, 1223–1236, doi: [10.1111/j.1365-246X.2010.04884.x](https://doi.org/10.1111/j.1365-246X.2010.04884.x).
- Rost, S., E. J. Garnero, Q. Williams, and M. Manga (2005). Seismological constraints on a possible plume root at the core-mantle boundary, *Nature* **435**, 666–669, doi: [10.1038/nature03620](https://doi.org/10.1038/nature03620).
- Seton, M., R. D. Müller, S. Zahirovic, C. Gaina, T. Torsvik, G. Shephard, A. Talsma, M. Gurnis, M. Turner, S. Maus, *et al.* (2012). Global continental and ocean basin reconstructions since 200 Ma, *Earth Sci. Rev.* **113**, 212–270, doi: [10.1016/j.earscirev.2012.03.002](https://doi.org/10.1016/j.earscirev.2012.03.002).
- Tackley, P. J. (2011). Living dead slabs in 3-D: The dynamics of compositionally-stratified slabs entering a “slab graveyard” above the core-mantle boundary, *Phys. Earth Planet. In.* **188**, 150–162, doi: [10.1016/j.pepi.2011.04.013](https://doi.org/10.1016/j.pepi.2011.04.013).
- Thorne, M. S., and E. J. Garnero (2004). Inferences on ultralow-velocity zone structure from a global analysis of SPdKS waves, *J. Geophys. Res.* **109**, doi: [10.1029/2004JB003010](https://doi.org/10.1029/2004JB003010).

- Thorne, M. S., E. J. Garnero, G. Jahnke, H. Igel, and A. K. McNamara (2013). Mega ultra low velocity zone and mantle flow, *Earth Planet. Sci. Lett.* **364**, 59–67, doi: [10.1016/j.epsl.2012.12.034](https://doi.org/10.1016/j.epsl.2012.12.034).
- Thorne, M. S., K. Leng, S. Pachhai, S. Rost, C. W. Wicks, and T. Nissen-Meyer (2021). The most parsimonious ultralow-velocity zone distribution from highly anomalous SPdKS waveforms, *Geochem. Geophys. Geosys.* **22**, doi: [10.1029/2020GC009467](https://doi.org/10.1029/2020GC009467).
- Thorne, M. S., S. Pachhai, K. Leng, J. K. Wicks, and T. Nissen-Meyer (2020). New candidate ultralow-velocity zone locations from highly anomalous SPdKS waveforms, *Minerals* **10**, 211, doi: [10.3390/min10030211](https://doi.org/10.3390/min10030211).
- Thorne, M. S., N. Takeuchi, and K. Shiomi (2019). Melting at the edge of a slab in the deepest mantle, *Geophys. Res. Lett.* **46**, 8000–8008, doi: [10.1029/2019GL082493](https://doi.org/10.1029/2019GL082493).
- Vanacore, E. A., S. Rost, and M. S. Thorne (2016). Ultralow-velocity zone geometries resolved by multidimensional waveform modeling, *Geophys. J. Int.* **206**, 659–674, doi: [10.1093/gji/ggw114](https://doi.org/10.1093/gji/ggw114).
- Walter, M. J. (2021). Water transport to the core-mantle boundary, *Natl. Sci. Rev.* **8**, doi: [10.1093/nsr/nwab007](https://doi.org/10.1093/nsr/nwab007).
- Wicks, J. K., J. M. Jackson, W. Sturhahn, and D. Zhang (2017). Sound velocity and density of magnesiowüstites: Implications for ultralow-velocity zone topography, *Geophys. Res. Lett.* **44**, 2148–2158, doi: [10.1002/2016GL071225](https://doi.org/10.1002/2016GL071225).
- Williams, Q., and E. J. Garnero (1996). Seismic evidence for partial melt at the base of earth's mantle, *Science* **273**, 1528–1530.
- Wolf, J., M. D. Long, and D. A. Frost (2024). Ultralow velocity zone and deep mantle flow beneath the Himalayas linked to subducted slab, *Nature Geosci.* doi: [10.1038/s41561-024-01386-5](https://doi.org/10.1038/s41561-024-01386-5).

Manuscript received 5 February 2024

Published online 13 May 2024